PCCP

In situ STM study of electrodeposition and anodic dissolution of Ni on Ag(111)

A. Lachenwitzer,† S. Morin,‡ O. M. Magnussen and R. J. Behm

Abteilung Oberflächenchemie und Katalyse, Universität Ulm, 89069 Ulm, Germany

Received 12th April 2001, Accepted 25th June 2001
First published as an Advance Article on the web 25th July 2001

A study of the electrodeposition and electrochemical dissolution of ultrathin Ni films on Ag(111) electrodes in Watts electrolyte by *in situ* scanning tunneling microscopy (STM), electrochemical quartz microbalance (EQCM), and cyclic voltammetry (CV) is presented. Ni deposition starts at potentials negative of -0.72 V *vs.* SCE (*i.e.*, overpotentials $\eta \geqslant 160$ mV), where an incommensurate, (111)-oriented film with an in-plane lattice rotation of 0.5° relative to the Ag substrate lattice is formed. The lateral nearest neighbor spacing is as in bulk Ni (2.49 Å) for a film thickness $\geqslant$3 ML and expanded for monolayer (2.54 Å) and bilayer (2.52 Å) films. Depending on the deposition potential, three growth regimes, resulting in different deposit morphologies, are observed: At low overpotentials ($160 \leqslant \eta$/mV $\leqslant 200$) a smooth Ni film is formed *via* a 2D step-flow growth process, commencing at steps of the Ag substrate. At medium overpotentials ($200 \geqslant \eta$/mV $\geqslant 300$) a transformation from 2D step-flow to 3D growth occurs, resulting in the selective formation of Ni multilayer islands along the Ag steps. At even higher overpotentials ($\eta \geqslant 300$ mV) 3D islands are formed at the steps and on the substrate terraces. The size of the Ni multilayer islands is independent of the terrace widths, indicating that Ni growth proceeds *via* direct discharge at step sites ("direct deposition"). The transition from 2D to 3D growth as well as the change in island shape with overpotential can be rationalized by a different potential dependence of the various microscopic nucleation and growth processes. The multilayer growth at steps is attributed to next-layer nucleation at the structural defect induced by the Ag–Ni boundary and can be described quantitatively as a function of deposition time by a simple 2D model. In addition, place-exchange of Ni with Ag surface atoms and encapsulation of Ni islands by Ag is observed. Dissolution of the electrodeposited multilayer Ni films proceeds *via* step-flow etching, with a higher dissolution rate for the Ni monolayer as compared to higher Ni layers.

1. Introduction

The electrochemical deposition of nickel is an important, well-established technical process. Although it has been used mainly for protective coatings on stainless steels and other materials, new applications for electrochemical Ni deposition have emerged recently. These applications include steps in the production of micro-mechanical devices, the manufacturing of magnetic recording heads, and the deposition of ultra-thin films for magnetic sensors. These applications require a better control of the structure and the morphology of the Ni deposits and of the deposition process. Here we report *in situ* STM results on the electrodeposition and dissolution of Ni on Ag(111) as part of an ongoing systematic study of ultra-thin, epitaxial Ni films on single-crystalline metal electrodes by our group.[1–8]

Previous studies of Ni electrodeposition mainly focused on the electrochemical behavior and on the micrometre-scale morphology of Ni deposits on carbon and various metallic substrates and their dependence on the deposition conditions,[9–30] such as temperature and stirring,[9] the nature of the substrate[18] and the electrolyte composition.[15,19] Regarding the latter, in particular the role of boric acid as a component in the widely-utilized Watts electrolyte has been studied,[12,26] which is conventionally believed to act as a buffer in the near-surface region and thus prevents the formation of metal hydroxide precipitates.[31,32] On the other hand, it has also been suggested that it influences the deposition by adsorption on the surface[12,30] or acts as a homogeneous catalyst for Ni deposition *via* formation of an intermediate Ni complex.[26,27] Furthermore, the effect of pH on Ni electrodeposition at low Ni(II) concentrations[19–21] and the effects of additives, such as brighteners[28,29] have been investigated. In addition, kinetic data were obtained by EQCM[23,25,33–35] and electrochemical impedance spectroscopy (EIS)[15,20] studies, which revealed a pronounced dependence of the current efficiency for Ni deposition on the overpotential due to the coevolution of hydrogen in the deposition regime.

For better insights into the atomic and nanometre-scale structure as well as into the growth and dissolution processes the electrodeposition of Ni on Au,[1–5,36] Ag[6,7,37] and other substrates[8,38,39] has been studied by *in situ* STM. In particular, a detailed STM study of the electrodeposition and electrochemical dissolution of Ni on reconstructed Au(111) electrode surfaces in various electrolytes demonstrated the electrochemical formation of well-defined, ultra-thin, epitaxial Ni films, revealing a complex nucleation and growth behaviour that depends strongly on the deposition potential.[1–3,5] Formation of Ni nuclei started below the Ni^0/Ni^{2+} equilibrium Nernst potential *via* place exchange of Ni with Au atoms at the elbows of the herringbone reconstruction, followed by nucleation of Ni islands on top of these substitutional Ni atoms at overpotentials $\eta \geqslant 80$ mV, and by nucleation at step edges of the Au substrate at $\eta \geqslant 100$ mV.[1] At submonolayer coverages, islands with two different growth morphologies were

† Present address: Department of Chemistry and Biochemistry, University of Guelph, Guelph, ON, Canada N1G 2W1.
‡ Present address: Department of Chemistry, York University, Toronto, ON, Canada M3J 1P3.

observed: compact, triangularly shaped islands and highly anisotropic, needle-like islands.[2] Upon further growth these islands coalesce to form an almost perfect two-dimensional Ni monolayer.[3] Multilayer growth up to coverages of 7 ML exhibits a layer-by-layer growth, resulting in very smooth Ni films. Complementary EQCM studies found 10–20 times higher growth rates and different Tafel slopes for the Ni monolayer as compared to the multilayer, suggesting that on the Ni deposit the ion discharge reaction is inhibited by adsorbates.[35] Atomic-scale STM observations revealed a hexagonal Ni lattice with a lattice spacing of 2.5 Å, similar to the (111) orientation in bulk Ni, and with the same orientation as the Au lattice.[3] The order in the highly defective first layer is considerably improved by second-layer deposition. Dissolution of these Ni films at potentials positive of the Nernst potential proceeds *via* formation of 3D etch pits that reach all the way down to the Au substrate, followed by lateral growth of these pits.[3] Furthermore, Ni underpotential deposition was reported in the presence of sulfamate anions; this was attributed to the complexation of Ni cations by sulfamates adsorbed on the surface.[36] The significant differences with respect to vapor-deposited Ni on Au(111) indicate a structure-decisive role of coadsorbates in the electrochemical environment.[5] Ni deposition on a Au(100) surface shows pronounced differences in the mechanisms of nucleation and submonolayer growth on the reconstructed and the unreconstructed surfaces and in the minimal overpotentials required for deposition ($\eta_{rec} = 100$ mV, $\eta_{unrec} = 40$ mV). The different growth mechanisms and resulting morphologies were rationalized by the different surface mobility and different mechanisms of strain release in the Ni deposit, in particular the incorporation of Au atoms into the Ni deposit in the case of the reconstructed substrate. At multilayer coverages a rough morphology evolves on reconstructed as well as unreconstructed Au(100). In summary, Ni deposition on Au(111) and Au(100) is strongly influenced by the presence of a reconstructed surface on these substrates, a phenomenon that seems to be unique to Au in the electrochemical environment. In contrast, much less is known about Ni electrodeposition on other, unreconstructed metal surfaces.

Here we report results of a detailed study on the electrodeposition of ultrathin Ni films on Ag(111) by *in situ* STM and complementary electrochemical and EQCM measurements. The mechanisms of nucleation and growth in the range of submonolayer coverages up to a few monolayers, the structure and morphology of the resulting deposit, and the anodic dissolution of the Ni films are described. The Ag substrate is particular interesting for the comparison with Au, since it exhibits almost identical lattice constants, resulting in a similar mismatch with the Ni lattice, but is unreconstructed. On the other hand, considerable electronic differences between Au and Ag exist, resulting in a significantly lower work function of Ag(111) and, correspondingly, a more negative potential of zero charge (pzc) as compared to Au(111)[40] as well as a higher enthalpy of mixing for Ni atoms in Ag than in Au data.[41] As will be shown below, similarities as well as characteristic differences to Ni nucleation and growth on Au(111) exist, which can be rationalized by these structural and electronic effects. In addition, Ni place exchange with Ag surface atoms and Ni-induced restructuring of the Ag substrate will be discussed. Several aspects of this work have been reported before[6,7,37] and will be only briefly reviewed here.

2. Experimental

The STM experiments were carried out in a home-built STM, described in detail in ref. 42. The tunneling tips were electrochemically etched in 2 M NaOH from a polycrystalline tungsten wire and subsequently coated with Apiezon wax. Tip and sample potential were independently kept under potentiostatic control, with the tip potential usually 50 to 150 mV more negative than the sample potential. Saturated calomel (SCE) or Ag/AgCl (KCl sat.) reference electrodes were used in the STM and electrochemical experiments, however, all potentials are reported *vs.* SCE. The Ag(111) single crystal samples were oriented, cut to $\pm 0.5°$, and mechanically polished with diamond paste down to 0.25 μm grain size. Prior to each experiment the sample was chemically polished using a CrO_3–HCl mixture as described in ref. 43 and 44 and then immersed under potential control at potentials between −0.1 and −0.2 V *vs.* SCE. The deposition experiments were performed in a modified Watts electrolyte, 10^{-3} M $NiSO_4$ + 10^{-2} M H_3BO_3 + 10^{-4} M HCl, prepared from suprapure H_3BO_3 and HCl, p.a. grade $NiSO_4$, and MilliQ-water. STM images were obtained in constant current mode (tunneling currents typically between 1 and 10 nA) and are presented as top view images with brighter colors corresponding to higher surface areas.

The CV's were obtained with a BAS CV-27 potentiostat in a separate cell on the same Ag(111) electrodes, using a hanging meniscus configuration. To avoid contributions from oxygen reduction, the cell was purged with nitrogen or argon (6.0). EQCM measurements were performed with a QCA917 quartz crystal analyzer (Seiko EG&G) coupled with the potentiostat on thin ($\approx$180 ML thick), epitaxial Ag films, electrodeposited on (111)-oriented Au films (mosaic spread 2° half width at half maximum) on quartz (9 MHz, AT-cut). The Ag films were 120 to 360 ML thick and deposited in the EQCM cell from 0.05 M H_2SO_4 + 5 × 10^{-3} M $AgNO_3$ solution at a rate of 0.1 to 0.2 ML s^{-1}, with the thickness of the Ag electrode being monitored *in situ* using the frequency change of the EQCM. Under these conditions a flat, (presumably relaxed) pseudomorphic Ag deposit should form in a layer-by-layer growth process.[45] After deposition of the Ag film the electrode was disconnected and the electrolyte was replaced by 0.1 M H_2SO_4 solution. Subsequently, a potential of 0.02 V *vs.* SCE was applied and the H_2SO_4 solution was exchanged under potential control by modified Watts electrolyte. More details on the experimental set-up for the EQCM experiments are given in ref. 35 and 42.

3. Results

3.1. Cyclic voltammetry and EQCM studies

Prior to the STM measurements, the electrodeposition of Ni on Ag(111) was characterized by cyclic current–voltage curves (CVs). A typical voltammogram for bare Ag(111) in 10^{-3} M HCl is shown in Fig. 1a (dotted curve). The predominant features of this voltammogram are (i) the pair of reversible peaks observed at about 0.03 V *vs.* SCE (I/I′), which are attributed to a disorder–order phase transition in the adsorbed chloride layer[46–48] and (ii) the large cathodic current negative of −0.6 V *vs.* SCE caused by hydrogen evolution. In the Watt's electrolyte, the features in the CVs are modified (Fig. 1a, solid curve). Sweeping the potential down to −0.68 V, *i.e.*, significantly negative of the reversible potential for the Ni^0/Ni^{2+} couple as determined from the Nernst equation (−0.56 V *vs.* SCE, see arrow in Fig. 1b), does not result in detectable Ni deposition. Instead, two pairs of reversible peaks near 0.08 (II/II′) and −0.49 V *vs.* SCE (III/III′) are observed. Peaks II/II′ are attributed to the same phase transition in the Cl adlayer as suggested for peaks I/I′, with the changes in peak position, height, and width being predominantly caused by the lower concentration of Cl^-. The additional peaks III/III′, which are observed only in Ni^{2+} containing electrolyte, exhibit a peak potential of −0.49 V *vs.* SCE, *i.e.*, slightly positive of the Ni^0/Ni^{2+} equilibrium potential, and correspond to a charge of 8 μC cm^{-2}, independent of the potential sweep range (provided the potential is kept positive of the Ni deposition range). They are tentatively attributed to a phase transformation of a

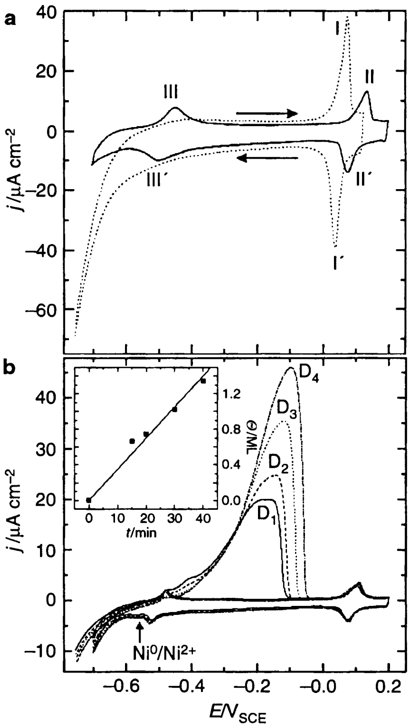

Fig. 1 Cyclic voltammograms (sweep rate 20 mV s^{-1}) of Ag(111) in (a) 10^{-3} M HCl (dotted line) and Watts electrolyte (full line); (b) Watts electrolyte after deposition at −0.75 V *vs.* SCE for 15 min (D_1, 399 μC), 20 min (D_2, 445 μC), 30 min (D_3, 612 μC) and 40 min (D_4, 803 μC), (sweep rate 10 mV s^{-1}), in the inset the Ni coverage Θ, evaluated from the Ni dissolution charges is plotted (average deposition rate 0.035 ± 0.001 ML min^{-1} indicated by solid line).

surface species involving either a relatively small change in coverage or small partial charge transfer. A possible explanation could be the formation of an adsorbed Ni-containing species as a precursor of Ni deposition. The latter was observed for Ni deposition on Cu(100) in Watts electrolyte,[8] for Ni deposition on Au(111) in sulfamate-containing solution[36] as well as suggested in previous electrochemical studies, where the adsorbed species was thought to involve chloride[49] or hydroxylated nickel complexes.[20,21] Direct evidence for the existence of such adsorbates, however, was not found in our STM studies (see below) nor did we see evidence for such an adsorption step in the EQCM results (see below).[42]

On Ag(111) Ni bulk deposition starts at potentials negative of −0.72 V *vs.* SCE, *i.e.*, at an overpotential η of ≈160 mV. Due to the large overpotential required for this process, the Ni electrodeposition current is masked by the current for hydrogen evolution and hence, no distinct Ni deposition peak can be resolved in the CV experiments. The amount of deposited Ni is therefore inferred from the Ni dissolution current in the anodic potential scan. As can be seen in the CVs in Fig. 1b, which were obtained after polarization for different times (15 to 40 min) at −0.75 V *vs.* SCE (η = 190 mV), pronounced nickel dissolution peaks (D_1 to D_4) are observed at potentials positive of the Ni^0/Ni^{2+} Nernst potential, well above the hydrogen evolution range. The precise peak potential depends on the amount of deposited Ni and on the scan rate, but the onset of Ni occurs between −0.5 and −0.4 V *vs.* SCE. This behavior resembles closely that of Ni electrodeposition on Au.[3] Electrochemical quartz microbalance measurements (see below) indicate that virtually no hydrogen is incorporated into the Ni deposit for this range of overpotentials and electrolytes at pH 4.[42] Hence, integration of the dissolution current allows the direct evaluation of the Ni coverage as a function of the deposition parameters, assuming a two-electron transfer and a Ni(111)-like deposit structure. The inset in Fig. 1b shows the dependence of the coverage Θ on the deposition time t. Clearly, Θ increases linearly with time, resulting in a deposition rate of ≈0.035 ML s^{-1} at −0.79 V *vs.* SCE (η = 190 mV). It is noted that peak II is still present in the anodic potential scans as a shoulder at the onset of nickel dissolution for Ni coverages below 1 ML (Fig. 1b, solid line), but is increasingly reduced (in comparison to the cathodic scan) for coverages exceeding 1 ML. This strongly suggests that the corresponding process involves species that are adsorbed on the Ag surface rather than on the Ni deposit. Finally, the cyclic voltammogram of the Ni-free Ag electrode (Fig. 1a) is perfectly reproduced in subsequent potential cycles, suggesting that the Ag(111) surface is not significantly altered by the deposition and stripping of Ni.

In addition to the CVs on Ag(111) single crystals, EQCM and voltammetric experiments were performed on Ag thin film electrodes (Fig. 2). The CV obtained on such a film in the Watts electrolyte (Fig. 2a, dashed line) resembles that recorded on the Ag(111) single crystal. The weaker pair of peaks at ≈0.10 V *vs.* SCE (I/I′) is most likely related to anion adsorption, with the reduced current and broadening of these peaks probably being related to structural imperfections in the Ag film. More important, the CV exhibits a pronounced Ni dissolution peak at ≈ −0.4 V *vs.* SCE (D), starting at ≈ −0.5 V *vs.* SCE. The more negative potential of the peak maximum as

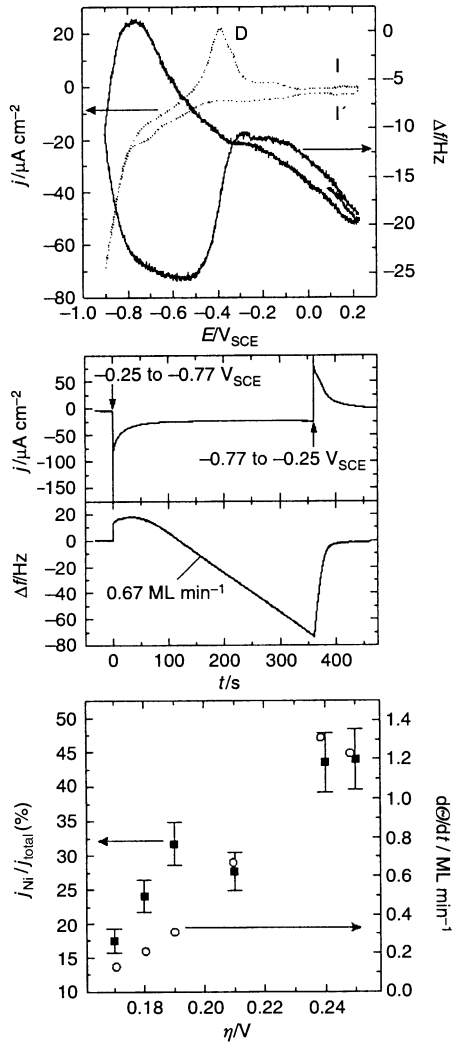

Fig. 2 (a) Cyclic voltammogram and corresponding EQCM-signal for an *in situ* prepared Ag covered quartz crystal in Watts electrolyte (10 mV s^{-1}),[35] see text for details. (b) Current and EQCM transient after a potential step into the regime of Ni deposition. (c) Ni deposition rate (circles) and current efficiency (filled squares), obtained from the linear growth regime of the EQCM transients, as a function of overpotential.

compared to the CVs on Ag(111) is attributed to kinetic effects (faster dissolution kinetics), caused by the larger defect density of the Ag films (see below). In the parallel recorded frequency change response (Fig. 2a, solid line) pronounced reversible frequency changes are found between −0.75 and 0.2 V *vs.* SCE, which indicate a decrease in mass with decreasing potential, probably due to desorption of anionic species. At more negative potentials a sharp decrease in frequency (*i.e.*, increase in mass) indicates the onset of Ni deposition (for the given experimental set-up 1 ML of a Ni(111) deposit corresponds to a frequency change of 27 Hz cm^{-2} according to the Sauerbrey equation[35]). The mass continues to increase even after the potential is reversed and only at ≈ −0.5 V *vs.* SCE does dissolution commence, in accordance with the CV. Potential-step experiments indicate that the onset of Ni deposition occurs at −0.73 V *vs.* SCE, in good agreement with CV and STM measurements on Ag(111) single crystal samples. An example of such an experiment, where the potential was stepped to −0.77 V *vs.* SCE, is shown in Fig. 2b. Obviously, the rate of Ni deposition is initially low, but continuously increases with time, until a steady state with a constant Ni deposition rate (0.67 ML min^{-1} in Fig. 2b) is reached after ≈80 s. This can be rationalized by the nucleation and growth behavior in this potential regime, which will be discussed in more detail in section 4.3. With increasing overpotential the deposition rate in the regime of constant growth ($\eta \leqslant 0.21$ V) first increases approximately exponentially with a Tafel slope of ≈58 mV (Fig. 2c). The saturation at deposition rates ⩾1 ML min^{-1} can be attributed to diffusion limitation, as shown in detail in ref. 35. In addition, these measurements indicate, as for Ni deposition on Au,[35] a continuous increase in the Ni deposition efficiency j_{Ni}/j_{total} with increasing overpotential from 17% at −0.73 V *vs.* SCE to 45% at −0.81 V *vs.* SCE (Fig. 2c).

3.2. STM studies

The microscopic surface structure and the Ni electrodeposition/dissolution processes were studied in detail by *in situ* STM. Two different strategies were employed in these studies: First, the growth (or dissolution) of Ni was directly followed by STM observations in the electrodeposition (or dissolution) regime. This is the preferred approach since it gives time-resolved data on the nucleation and growth process. At high overpotentials, however, such measurements are not possible due to the high rates of Ni deposition and due to pronounced hydrogen evolution, which destabilizes the STM tip. Hence, in this regime a second method was used, where Ni was deposited for defined times with the tip withdrawn (100–200 μm) and where the STM images were recorded subsequently in the potential regime between −0.70 and −0.60 V *vs.* SCE, *i.e.*, at potentials where the Ni deposit is stable and neither significant dissolution nor further growth occurs (deposition and imaging conditions are noted explicitly in the figure captions). In addition, experiments with this method at lower overpotentials verified that under those conditions the Ni deposition process is only slightly affected by the presence of the scanning tip in this potential regime (see below).

Due to the rather complex Ni nucleation and growth behavior on Ag(111), the data will be presented in several subsections: First, place exchange processes in the initial stages of Ni electrodeposition are discussed, followed by a description of Ni island nucleation and growth in three different overpotential regimes, and, finally, by observations on the anodic dissolution of the Ni deposit.

Place exchange during Ni electrodeposition. *In situ* STM images of freshly prepared Ag(111) electrodes in Watts electrolyte at potentials positive of −0.70 V *vs.* SCE (Fig. 3a and b) reveal extended, atomically smooth terraces separated by monoatomically high steps, which appear frizzy due to rapid

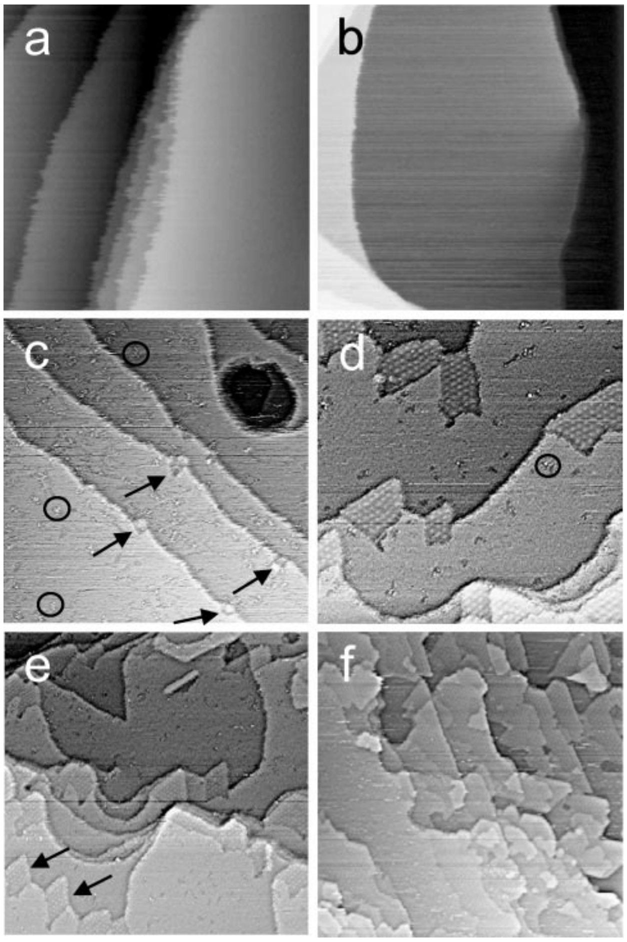

Fig. 3 (a, b) STM images of the bare Ag(111) surface (a) in 10^{-3} M HCl at −0.23 V *vs.* SCE (2020 × 2020 Å^2) and (b) in Watts electrolyte at −0.44 V *vs.* SCE (2800 × 2800 Å^2). (c–f) STM images of Ag(111), showing the surface morphology after experiments, where Ni was deposited from Watts electrolyte at low overpotentials. The images were recorded at (c–e) −0.74 V *vs.* SCE and (f) −0.73 V *vs.* SCE for various deposition times t_{dep}, the images were recorded at (c–e) −0.65 V *vs.* SCE and (f) −0.73 V *vs.* SCE. (c) t_{dep} = 3 min (1000 × 1000 Å^2); (d) t_{dep} = 7 min (1000 × 1000 Å^2); (e) t_{dep} = 7 min (1300 × 1300 Å^2); (f) t_{dep} = 40 min (2000 × 2000 Å^2).

kink motion along the step edge. These observations are in good agreement with previous results obtained on Ag(111) in sulfuric acid solution.[50,51] Upon changing the potential into the Ni deposition range, small features, which manifest in the STM images as apparent "holes", emerge on the Ag terraces. Examples, recorded after deposition at −0.74 V *vs.* SCE (η = 180 mV), are visible in Fig. 3c and d (marked with circles). These "holes" have diameters between 20 and 50 Å, a surface density of ≈10^{12} cm^{-2}, apparent depths of 0.3 to 0.6 Å, and often exhibit small protrusions along their edges. They are observed only in Ni-containing electrolyte after the potential was kept in the range of Ni deposition and were not found on the surface after complete dissolution of the Ni deposit. As for similar STM observations of Ni on Ag(111) under UHV conditions[52] and Ni on Au(111) in UHV[53,54] and an electrochemical environment,[1,3] these features are assigned to substitutional Ni atoms that have replaced Ag surface atoms *via* a place exchange reaction. Since no Ag island formation is observed on the terraces, the expelled Ag atoms have to be redeposited at steps. For Ni deposition under UHV conditions[52] Ni islands (on top and substitutional Ni) are, at room temperature partially and at 600 K completely, covered by a Ag layer.[52] Also in the electrochemical environment a certain, although smaller, tendency towards Ni encapsulation is found (see below), which is supposed to be the driving force for the observed place exchange processes. The differences to the UHV system may be caused, *e.g.*, by the presence of adsorbates, such as anions, on the electrode surface.

Ni deposition at low overpotential (160 mV $\leqslant \eta \leqslant$ 200 mV). The initial stages of Ni deposition on Ag(111) at potentials close to the onset of Ni deposition ($\eta \geqslant$ 160 mV), where the Ni growth rate is low, are illustrated by the STM images in Fig. 3c–f. After 3 min of deposition at -0.74 V *vs.* SCE (Fig. 3c) only a few Ni islands are observed, which nucleate exclusively at the lower side of the Ag substrate steps (see black arrows). This differs from deposition under UHV conditions, where nucleation of Ni islands not only occurs at the Ag steps, but also on the terraces, either by homogeneous nucleation or by heterogeneous nucleation on top of substitutional Ni atoms formed by the place exchange reaction.[52] Possible reasons for the nucleation behavior observed at the electrochemical interface, and in particular for the absence of nucleation on top of place exchange sites, will be discussed later. With increasing deposition time, the Ni islands increase in size and number (Fig. 3d and e). They can be distinguished from the Ag substrate by their characteristic long-range modulation pattern (see below). Interestingly, the islands do not simply grow along the Ag steps and onto the terraces, but appear to grow into the upper terrace, as illustrated by the diamond-shaped Ni islands in Fig. 3e (see arrows). Furthermore, after deposition new morphological features appear, such as pits and "fjords" in the terraces, which are not observed at these potentials in the absence of Ni^{2+} in the electrolyte. Both effects resemble similar observations for Ni on Ag(111) under UHV conditions[52] and originate from a restructuring of the Ag substrate steps during Ni growth, leading to partial Ni island encapsulation, and are discussed in detail in ref. 37.

For longer deposition times a quasi layer-by-layer growth of the Ni deposit is observed at this potential (Fig. 3f). Second-layer Ni islands are formed due to growth of first-layer Ni islands on the upper terrace across descending steps, covering Ni monolayer islands on the lower terrace, or *via* nucleation on top of the Ag–Ni boundary and at the edges of first layer Ni islands (see below). The rates of these processes, however, are so low that Ni deposition proceeds (at least in the range of the Ni film thickness of 3 to 4 layers studied here) effectively *via* layer-by-layer growth. As a result rather smooth deposits are formed in this potential regime, as illustrated in Fig. 4a for a 2 ML Ni deposit, obtained after 15 min deposition at -0.75 V *vs.* SCE. The Ni film is not completely uniform, but exhibits holes which reach down to the Ag substrate (easily recognizable by the absence of the long-range pattern, see white arrows) and which are primarily located in the centers of extended Ag terraces. They are caused by the almost exclusive formation of first and higher layer islands at the Ag steps and the slow lateral growth of Ni islands (see also next section). The steps of the Ni deposit exhibit straight sections of up to several hundred Å in length, which are oriented parallel to the long-range modulation pattern (see also Fig. 10a), *i.e.*, tend to be oriented along the close-packed directions of the Ni lattice (see below).

High-resolution STM images (Fig. 4b), obtained on the bilayer island in the center of Fig. 4a, reveal a hexagonal atomic lattice with a nearest-neighbor spacing of 2.5 Å, *i.e.*, close to that of (111)-oriented bulk Ni. It is superimposed by a well-ordered long-range modulation, which is slightly rotated ($\alpha = 5° \pm 0.5°$) relative to the atomic Ni lattice. The latter corresponds to a moiré pattern, resulting from the lattice mismatch between the Ag substrate lattice and the Ni adlattice. The vertical modulation amplitude is rather high for mono- and bilayer films (0.6 Å according to the cross-section in Fig. 4c), but decreases with increasing film thickness (third Ni layer: $\approx$0.4 Å, fourth Ni layer: $\approx$0.2 Å) and almost completely vanishes for thicker deposits (>7 ML). The moiré lattice spacing Λ decreases from 21 $\pm$ 0.5 Å for Ni monolayers to 19.5 $\pm$ 0.5 Å for bilayer Ni films and 18 $\pm$ 0.5 Å for thicker multilayer deposits (average values obtained on different islands from drift-corrected STM images). The observed differences in Λ are well above the standard deviations for the distances measured for a given layer thickness. They hence have to be attributed to a systematic dependence of Λ on the number of Ni layers, indicating a Ni lattice expansion with decreasing film thickness (see section 4.2). On the larger scale the moiré pattern is very well ordered and largely free of defects such as domain boundaries (see Fig. 4a). However, a few dislocations are observed, which result in a long-range distortion of the hexagonal pattern (see black arrow in Fig. 4a). A more detailed discussion of the Ni lattice structure will be given in section 4.2.

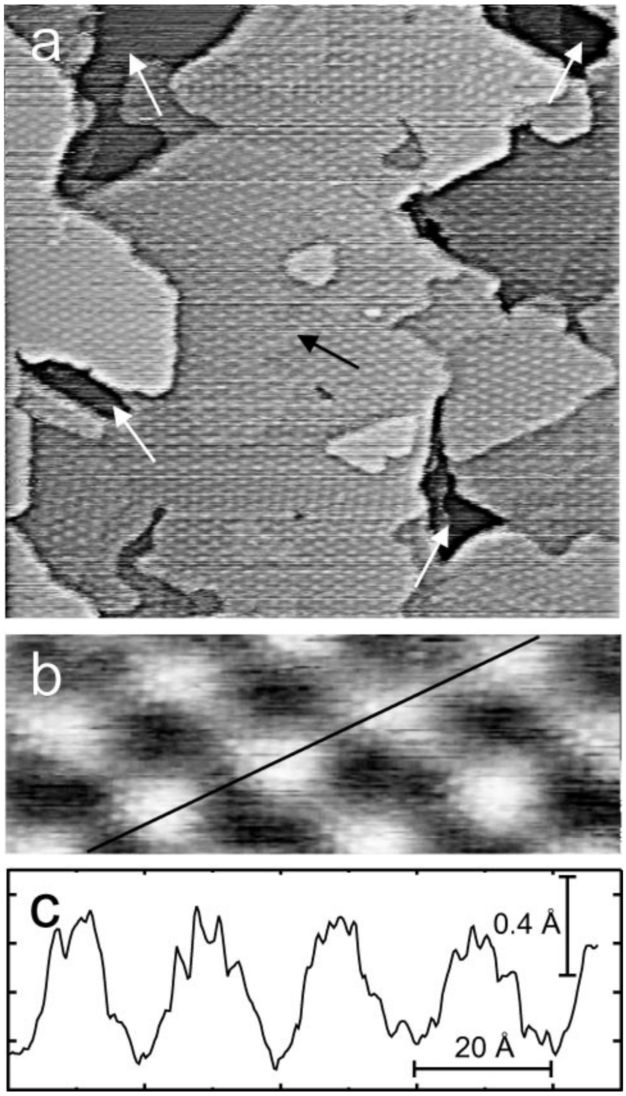

Fig. 4 (a) STM image of a Ni multilayer deposit on Ag(111) deposited for t_{dep} = 15 min at -0.75 V *vs.* SCE (1000 × 1000 $Å^2$, image recorded at -0.65 V *vs.* SCE, 2 ML average thickness). (b) Atomic resolution STM image obtained the Ni bilayer island in the center of the image in (a), showing the atomic Ni lattice and (c) cross-section through the maxima of the moiré pattern (indicated by the black line in (b)).

Ni deposition at medium overpotential ($\eta \geqslant$ 200 mV). Decreasing the deposition potential by only $\approx$40 mV (from $\eta \approx$ 160 mV to $\eta \approx$ 200 mV) leads to significant changes in the deposit morphology and a crossover from quasi two-dimensional step flow to three-dimensional step decoration growth. Fig. 5 shows time-resolved STM observations of Ni deposition at -0.77 V *vs.* SCE (η = 210 mV). At this potential the deposition still proceeds sufficiently slowly to allow *in situ*

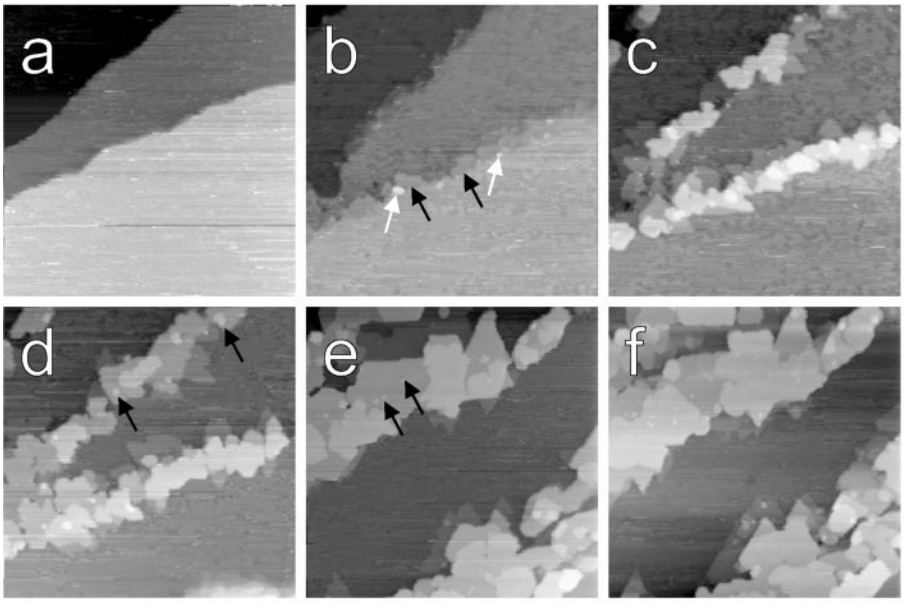

Fig. 5 STM images from a series of images recorded successively in the same area during Ni deposition on Ag(111) in the Watts electrolyte, showing the nucleation and growth of Ni multilayer islands at Ag steps (1350 × 1350 Å^2). (a) Initial surface at -0.44 V *vs.* SCE; (b) $t_{dep} = 2$ min at -0.77 V *vs.* SCE ($\Theta \approx 0.07$ ML); (c) $t_{dep} = 6$ min at -0.77 V *vs.* SCE ($\Theta \approx 0.46$ ML); (d) $t_{dep} = 8$ min at -0.77 V *vs.* SCE ($\Theta \approx 0.76$ ML); (e) $t_{dep} = 15$ min at -0.77 V *vs.* SCE ($\Theta \approx 0.95$ ML); (f) $t_{dep} = 16$ min at -0.77 V *vs.* SCE followed by 1 min at -0.79 V *vs.* SCE ($\Theta \approx 1.16$ ML).

monitoring of the nucleation and growth process. As for low overpotentials, Ni deposition starts with place exchange on the terraces and lateral growth of Ni nuclei at the lower terrace side of the Ag steps (Fig. 5b, indicated by black arrows). Almost simultaneously, however, second-layer Ni islands nucleate at the boundary between these Ni monolayer islands and the upper Ag terrace (white arrows). With increasing deposition time (Fig. 5c–f) the Ni islands grow laterally as well as in height. In a similar process (heterogeneous) nucleation of next-layer Ni islands again occurs, up to the fourth layer, predominantly at the position of the one-dimensional Ni–Ag boundary (see black arrows in Fig. 5d and e). In addition, next-layer nuclei are also formed at the edges of the underlying Ni islands, but to a much smaller extend. The rate for next-layer (heterogeneous) nucleation is initially high, but decreases continuously with increasing island height. This is concluded from the increasing size the top layer can reach before next-layer nucleation occurs ($\approx$50 Å for second layer, $\approx$200 Å for fifth layer), which is a measure for the next-layer nucleation probability due to the constant Ni deposition rate. A more quantitative description is given in Fig. 6, where the average height $\langle h \rangle$ and the aspect ratio $\langle w \rangle / \langle h \rangle$ of the Ni islands, evaluated from the time-resolved STM observations partly shown in Fig. 5, is plotted as a function of the deposition time. The values $\langle w \rangle$ and $\langle w \rangle / \langle h \rangle$ are calculated from the measured average height $\langle h \rangle$ and the total Ni coverage per unit step length Θ' *via*:

$$\langle w \rangle = \frac{\Theta'}{\langle h \rangle}$$

$$\frac{\langle w \rangle}{\langle h \rangle} = \frac{\Theta'}{\langle h \rangle^2}$$

The observed growth behavior can be rationalized by a simple model, which is described in detail in section 4.3 and in the Appendix.

As a consequence of this behavior characteristic deposit morphologies as shown in Fig. 7 evolve in this overpotential range. Obviously, Ni is deposited exclusively along the Ag steps, whereas the inner parts of wider terraces are completely free of Ni islands. The width and height of the wire-like Ni deposit is rather uniform, as illustrated by the large-scale image in Fig. 7a, where the islands are, on average, 8 Å high and 150 Å wide. In particular, it is independent of the size of the adjacent Ag terraces, which can be rationalized only if material transport from the terraces to the steps is not significantly limiting for the growth of these islands. On a smaller scale (Fig. 7b and d) it is clearly discernible that the quasi-1D deposits along the steps consist of individual, closely-spaced Ni multilayer islands. The shape of these islands is mesa-like, *i.e.*, they exhibit a "trapezoidal" cross-section with steep walls and a flat top (see line scan in Fig. 7c), which strongly differs from that expected for a simple kinetically controlled growth of multilayer islands. In addition, the STM images again indicate restructuring of the Ag substrate, resulting in the formation of fjords in the terraces (Fig. 7d, arrows).[37]

For longer deposition times the Ni multilayer deposit growth predominantly laterally. As an example, a large scale image of a $\approx$4 ML Ni deposit is shown in Fig. 7e, where the smaller terraces are completely covered by the Ni multilayer film and only the centers of larger terraces still exhibit the bare Ag substrate (examples marked with arrows). The closed Ni multilayer film is apparently relatively smooth and of rather uniform thickness ($\approx$6–8 ML). The Ni coverage in the

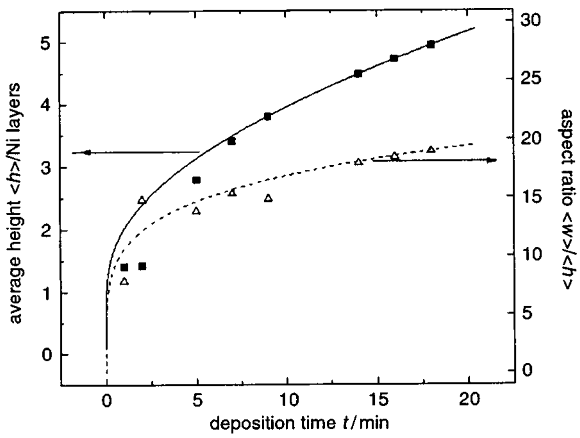

Fig. 6 Average Ni island height $\langle h \rangle$ (■) and island aspect ratio $\langle w \rangle / \langle h \rangle$ (△) as function of time and Ni coverage for deposition at -0.77 V *vs.* SCE, evaluated from the series of STM images partly shown in Fig. 5. In addition, the results of fits to a simple kinetic model of Ni island growth (see text) are shown (solid and dotted lines).

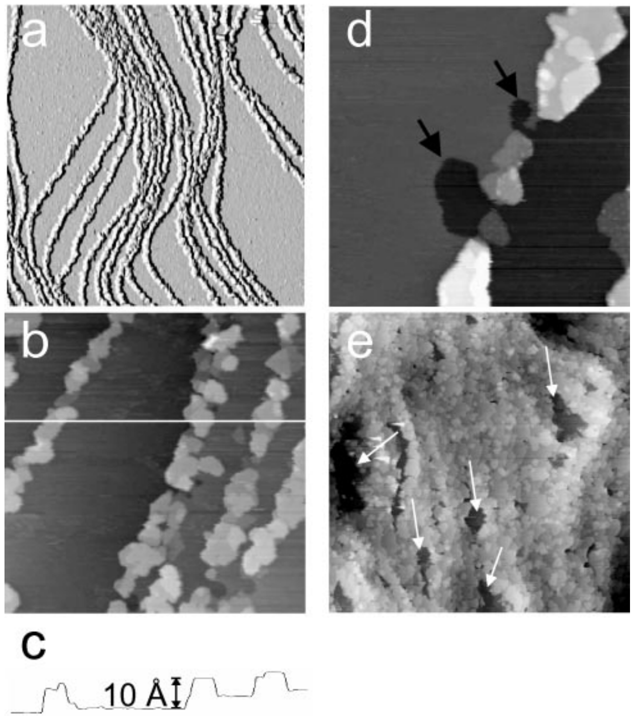

Fig. 7 STM images of the multilayer Ni deposit on Ag(111) formed at medium overpotential in Watts electrolyte and subsequently recorded at (a) −0.70 V *vs.* SCE or (b–e) −0.68 V *vs.* SCE. (a) t_{dep} = 20 min at −0.72 V *vs.* SCE followed by t_{dep} = 2 min at −0.77 V *vs.* SCE (8500 × 8500 Å^2, Θ = 1.0 ML); (b) t_{dep} = 4 min at −0.77 V *vs.* SCE (2000 × 2000 Å^2, Θ = 1.0 ML); (c) line scan at the position marked by the white line in (b); (d) t_{dep} = 5 min at −0.77 V *vs.* SCE (1200 × 1050 Å^2, Θ = 1.0 ML); (e) t_{dep} = 15 min at −0.78 V *vs.* SCE (8000 × 8000 Å^2, Θ > 4.0 ML).

image in Fig. 7e is higher than that in Fig. 5f, which was recorded under similar conditions *in situ* during Ni growth. This may be related to a lower local step density in the latter case or, less likely (see below), a slight shielding of Ni diffusion to the electrode by the scanning tip.

Quantitative evaluations of the coverage Θ as a function of deposition time t are presented in Fig. 8 for three deposition potentials. In all cases an approximately linear dependence is found. The data at η = 210 mV (squares) and η = 170 mV (circles) were obtained from a series of STM images recorded *in situ* during deposition and evaluated by integration of height and area of the Ni islands. They yield deposition rates $d\Theta/dt$ of 0.089 ± 0.005 ML min^{-1} and 0.014 ± 0.001 ML min^{-1}, respectively. For comparison, the data shown in Fig. 1b, obtained by cyclic voltammetry on the same Ag(111) crystal, are reproduced in Fig. 8 (triangles), which give a rate of 0.035 ± 0.001 ML min^{-1} for η = 190 mV. Hence, the STM and electrochemical results are in good agreement, indicating the absence of strong tip shielding effects. A plot of ln($d\Theta/dt$) *vs.* E suggests a Tafel slope of ≈50 mV for Ni deposition on Ag(111), in good agreement with more detailed kinetic studies.[55] A similar analysis for the growth rate of each Ni layer reveals that at η = 170 mV the average lateral growth rates of the first Ni layer $k_{Ag/Ni}$ is a factor 11 higher than that of the second and following layers $k_{Ni/Ni}$, whereas at η = 210 mV these rates are almost equal ($k_{Ag/Ni}/k_{Ni/Ni}$ = 1.7). This indicates a different potential-dependence for Ni layer growth on the Ni deposit as compared to that on the Ag substrate, which also will be discussed in section 4.3.

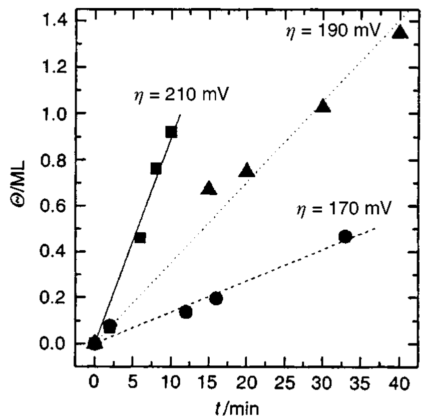

Fig. 8 Coverage Θ *vs.* time plots for overpotentials η = 210 mV (■), evaluated from the STM series shown in Fig. 5 (deposition rate 0.089 ± 0.005 ML min^{-1}), η = 170 mV (●), evaluated from a similar STM series (deposition rate 0.014 ± 0.001 ML min^{-1}), and η = 190 mV (▲), evaluated from the charges of the Ni dissolution peaks in Fig. 1b (deposition rate: 0.035 ± 0.001 ML min^{-1}).

Ni deposition at high overpotential ($\eta \geq$ 300 mV). The growth behavior at overpotentials ≥300 mV closely resembles that observed at medium overpotentials, except that for longer deposition periods, in addition to the preferred nucleation and growth of 3D islands at the Ag steps, Ni island formation also occurs in the center of terraces (Fig. 9). Due to the higher deposition rates, already 10 s deposition at −0.89 V *vs.* SCE (η = 330 mV) results in significant step decoration (Fig. 9a) with Ni islands of, on average, 40 Å width and one or two Ni layers height. In the initial stage of deposition only a few isolated islands (marked by arrows) are formed on the Ag terraces. After 30 s deposition at this potential (Fig. 9b and c), resulting in a total Ni coverage of ≈1 ML, the amount of islands on the terraces has substantial increased (1.2 × 10^{11} cm^{-1} average density in the center of larger terraces). Possible nucleation mechanisms, responsible for the formation of these islands in this potential regime, will be discussed below (section 4.3). The islands at the steps and on the terraces in Fig. 9b and c exhibit a mesa-like shape with an almost "rectangular" cross-section (see also the cross-section shown in Fig. 9d). The island size distribution of the islands on the terraces is considerably broader than that of the islands at the steps, which is attributed to differences in the nucleation

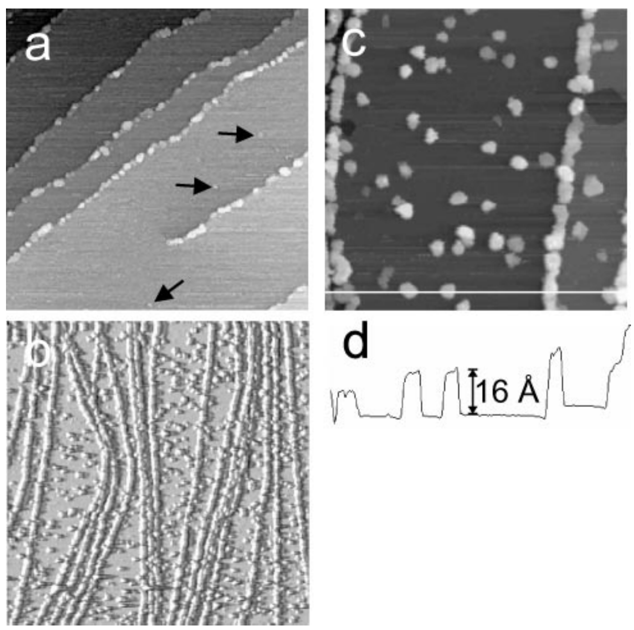

Fig. 9 STM images of the multilayer Ni deposit on Ag(111) formed at high overpotentials in the Watts electrolyte and subsequently recorded at (a) −0.68 V *vs.* SCE and (b, c) −0.67 V *vs.* SCE. (a) t_{dep} = 10 s at −0.89 V *vs.* SCE (2000 × 2000 Å^2, Θ = 0.2 ML), (b, c) t_{dep} = 30 s at −0.89 V *vs.* SCE ((b) 8500 × 8500 Å^2, (c) 2000 × 2000 Å^2, Θ = 1.0 ML); (d) line scan at the position marked by the white line in (c).

behavior. Whereas for the latter islands a saturation density of island nuclei is formed at high overpotentials in the first seconds of the deposition process (see Fig. 9a), the former nucleate more progressively, with the larger islands being formed in the earlier stages of deposition. The average height $\langle h \rangle$ and diameter $\langle w \rangle$ are 15 Å (corresponding to 7 to 8 Ni layers) and 100 Å for the islands at the steps and 14 and 130 Å for the islands on the terraces, respectively, indicating that although the nucleation rate on the terrace is initially slower, these islands (on average) grow faster. This can be rationalized by the significantly lower island density on the terraces as compared to that along the steps, which leads to a lower depletion of the Ni^{2+} ion concentration in front of the electrode surface and, correspondingly, to higher local growth rates of the islands on the terraces. Furthermore, comparison with the $\langle w \rangle$ and $\langle h \rangle$ values for the islands at the step edges obtained at medium overpotentials for similar Ni coverages, reveals a decrease in aspect ratio and an increase in the slope of the island edges with increasing overpotential.

Ni dissolution. According to the CV and EQCM results in section 3.1, the dissolution of the Ni deposit commences at potentials between −0.45 and −0.4 V *vs.* SCE. The STM images in Fig. 10 were recorded during an experiment, where the potential was gradually increased, starting from a deposit consisting of extended one- or two-layer high Ni islands (recognizable by the moiré pattern on top). Noticeable Ni dissolution commenced between −0.45 (Fig. 10a) and −0.41 V *vs.* SCE (Fig. 10b). According to these images, the Ni deposit dissolves via a step flow mechanism, without formation of etch pits in the Ni layer. During dissolution dents are formed in the Ni island edges (see arrow in Fig. 10b), leading to considerable roughening of the initially smooth Ni steps during the dissolution process. At more positive potentials the dissolution rate increased, as illustrated by the dissolution of the Ni bilayer island in the upper half of the images, which is reduced ≈50% in size within 6 min (Fig. 10c and d). Under these conditions even the transient formation of small islands in front of the step edges can be observed (see black arrow in Fig. 10c). They can be rationalized by a highly non-uniform Ni removal along the step edges, which causes the separation of more

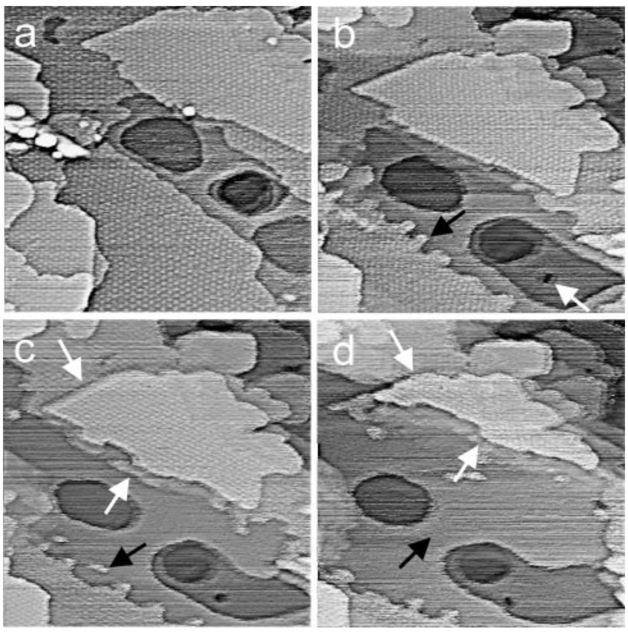

Fig. 10 STM images from a series of images recorded successively in the same area during anodic dissolution of the Ni deposit on Ag(111) in Watts electrolyte (900 × 900 $Å^2$). (a) −0.45 V *vs.* SCE, $t_{diss} = 0$ min; (b) −0.41 V *vs.* SCE, $t_{diss} = 18$ min; (c) −0.31 V *vs.* SCE, $t_{diss} = 28$ min; (d) −0.31 V *vs.* SCE, $t_{diss} = 34$ min.

stable areas from the main island. Interestingly, the dissolution of the first Ni layer is more rapid than that of the higher layers. This behavior is found at −0.45 V *vs.* SCE (Fig. 10a and b), where dissolution occurs almost exclusively at the first layer, as well as at −0.31 V *vs.* SCE (Fig. 10c and d, white arrows). It can be explained by a lower stability of Ni on Ag as compared to Ni on Ni, which will be discussed in more detail in section 4.4. As a consequence, dissolution of two-layer-high Ni islands proceeds by simultaneous removal of both Ni layers (*i.e.*, the bilayer step is maintained). Finally, as during Ni deposition, Ni dissolution is accompanied by restructuring of the Ag substrate. In particular, the ridge between the two holes in the Ag surface (marked with a black arrow in Fig. 10d) widens due to the incorporation of Ag atoms. The origin of this additional material will be addressed in the Discussion.

4. Discussion

4.1. Deposition overpotential and deposition rates

The three different methods used in this study, *in situ* STM, CV and EQCM, all find the onset of Ni deposition on Ag(111) at the same overpotential of ≈160 mV. This overpotential is significantly higher than that required for Ni deposition on Au(111) (80 mV[3]) although in both cases a (111)-oriented Ni film is formed. This indicates that the nucleation of Ni islands is kinetically more hindered on the Ag(111) substrate, which can be rationalized by two effects: First, the enthalpy of mixing for Ni atoms in the substrate metal is higher for Ag (+0.80 eV $atom^{-1}$) than for Au (+0.13 eV $atom^{-1}$),[41] suggesting that the energetic cost of the Ni/Ag interface is higher than that of the Ni/Au interface. Second, as also indicated by the anion desorption in the EQCM data, the potential of zero charge of Ag(111) (−0.7 V *vs.* SCE[40]) is significantly more negative than that of Au(111) (0.2 V *vs.* SCE[56]) and the deposition of a cationic complex should consequently be retarded on the former substrate.

The Ni deposition rate was measured by quantitative analysis of *in situ* STM data, voltammetric Ni stripping experiments, and EQCM. According to Fig. 9, a good correlation exists between the STM and the CV experiments for low coverages and overpotentials. Furthermore, the Tafel slopes estimated from the STM and CV data in Fig. 8 and the EQCM data in Fig. 2c are in good agreement. However, there is poor agreement between the absolute rates obtained by the two former methods and the EQCM experiments, which yield approximately seven times higher rates. This difference is most likely caused by the much higher roughness and heterogeneity of the Ag thin film samples used in the EQCM experiments as compared to the Ag(111) single crystal used in the other experiments.[35,42] Since Ni nucleation and growth occur preferentially at Ag steps, the increased roughness of the surface and the resulting higher step density should cause a correspondingly higher deposition rate. In view of this dependence on the surface morphology, it seems more meaningful to measure the deposition kinetics in rates that are normalized by the Ag step length, which can be easily done for those obtained from the *in situ* STM experiments. For the data shown in Fig. 8, we find $(3.3 \pm 0.2) \times 10^{-5}$ ML min^{-1} $Å^{-1}$ and $(2.6 \pm 0.2) \times 10^{-6}$ ML min^{-1} $Å^{-1}$ at $\eta = 210$ and $\eta = 170$ mV, respectively.

4.2. Structure of the deposited Ni film

The STM data clearly indicate a hexagonal atomic Ni lattice with a lattice spacing similar to that in bulk Ni and a well-defined orientation relative to the Ag(111) substrate lattice. Due to the lattice mismatch between Ni and Ag (nearest-neighbor spacings $d_{Ni} = 2.49$ Å, $d_{Ag} = 2.89$ Å, corresponding to 14% misfit), Ni atoms cannot occupy solely the energetically favored three-fold hollow sites of the substrate, but must also reside on the less-favorable bridge sites and on-top sites, resulting in a long-range vertical modulation. Analysis of this moiré pattern allows a precise determination of the admetal lattice structure. From the nearest-neighbor distance Λ of the moiré pattern maxima and the angle α between the Ni atomic rows and the rows of the moiré maxima the admetal atomic spacing d_{Ni} and rotation angle Ω relative to the substrate lattice are obtained *via*:[57]

$$\Lambda = \frac{d_{Ag} d_{Ni}}{\sqrt{d_{Ag}^2 + d_{Ni}^2 - 2 d_{Ag} d_{Ni} \cos \Omega}}$$

$$\alpha = \Omega + \arcsin\left(\frac{\Lambda}{d_{Ag}} \sin \Omega\right)$$

Using the Λ and α values obtained from Fig. 4b the rotational epitaxy angle of the Ni adlatice is evaluated to be $\Omega = 0.6° \pm 0.1°$. For small Ω and Λ/d_{Ag} ($\Omega < 1°$ and $\Lambda/d_{Ag} < 10$) these equations simplify to (relative error in d_{Ag}, Ω is $<0.1\%$):

$$d_{Ni} \approx \frac{d_{Ag} \Lambda}{d_{Ag} + \Lambda}$$

$$\Omega \approx \frac{\alpha}{1 + \Lambda/d_{Ag}}$$

With the first of these equations the dependence of the Ni nearest-neighbor spacing on the deposit thickness can be determined from the different moiré spacings, measured on Ni islands of different height. For three-layer-high (and higher) islands the average moiré spacing is 18 ± 0.5 Å, resulting in $d_{Ni} = 2.49 \pm 0.01$ Å, which is in good agreement with the bulk Ni spacing. In contrast, one- or two-layer-high islands exhibit moiré spacings Λ of 21 and 19.5 Å, corresponding to Ni–Ni distances of 2.54 and 2.52 ± 0.01 Å, respectively. These changes do not correspond to changes in the top Ni layer only (in that case two incommensurate interfaces, each with its own moiré spacing would result), but to a uniform change in the in-plane lattice spacing of the entire Ni film. The 4% expansion of the Ni monolayer relative to the Ni bulk can be rationalized by energetic contributions from the Ni/Ag and possibly the Ni/electrolyte interface, specifically from the balance between lattice strain and misfit energy. Deviations from bulk lattice spacings are also known for other ultra-thin metal films with incommensurate lattice structure deposited under UHV conditions systems[58] or electrochemically, *e.g.*, for the electrodeposition of Tl on Ag(111)[59] and Ag(100).[60] In the latter cases, however, the monolayer was not expanded as for Ni on Ag(111), but compressed with respect to thicker films or the admetal bulk. The different behavior most probably results predominantly from the different sign of the lattice misfit, which is negative for Ni on Ag(111) ($d_{Ni} < d_{Ag}$) but positive for the other systems. By relaxation of the admetal lattice towards a smaller misfit with the substrate lattice, the misfit energy can be reduced, an effect which is most dominant for monolayer deposits. In addition, energetic differences between these systems might play a role: whereas Tl on Ag(111) is an underpotential deposition (UPD) system, *i.e.*, the bonding between the Ag substrate and the Tl adlayer is stronger than the interaction between Tl adatoms, Ni adatoms interact less strongly with Ag than with Ni (see section 4.1). As a consequence, a higher admetal packing density is favored in the former system, but not in the latter. With increasing thickness the energy contribution due to Ni lattice strain dominates over that of the interface energy and the Ni lattice relaxes gradually to its bulk value. For Ni on Ag(111) as well as Tl UPD on Ag[59,60] the influence of the Ag/Ni interface on the lateral spacing effectively seem to be limited to the first two Ni layers. The moiré lattice modulation in contrast disappears only for island heights exceeding 5 to 6 layers, suggesting a slower relaxation with thickness of this vertical distortion.

In contrast to the electrochemical environment, where a moiré pattern is observed already on Ni monolayer islands, Ni islands deposited on Ag(111) under UHV conditions do not exhibit a moiré pattern up to the second layer reflecting pseudomorphic growth in the first two layers. This appears only in the third layer, with a spacing of ≈ 18 Å.[52] A similar difference exists also for Ni on Au(111), where a moiré pattern indicating a bulk-like Ni spacing is found on Ni monolayers formed by electrodeposition,[2,3] whereas monolayer islands deposited from the gas phase grow pseudomorphically.[61] Apparently, the presence of the electrolyte stabilizes the incommensurate Ni(111)-like structure. A possible explanation for this effect is a weakening of the Ni–substrate bond due to adsorption of electrolyte species (anions, water) on the Ni deposit.[2]

Despite the similar atomic scale structure, the morphology of the Ni deposit on Ag(111) and Au(111) differs strongly. On Ag(111) the moiré pattern is very well ordered and almost free of defects (*e.g.*, domain boundaries), apart from a few dislocations leading to a long-range distortion of the hexagonal pattern. In contrast, Ni monolayers formed by electrodeposition on Au(111) exhibit a highly defective moiré pattern indicating a high defect density.[3,6] The film thickness in this system, however, is much more uniform than on Ag(111), where holes in the Ni deposit reaching down to the substrate are frequently observed. The lower defect density and the less uniform thickness of the Ni deposit on Ag(111) can both be explained by the nucleation and growth behavior on these surfaces (see below): whereas Ni nucleation on Ag(111) is limited largely to the Ag steps, from where the nuclei grow laterally onto the terraces, nucleation on Au(111) can also occur within the terraces at elbows of the Au reconstruction,[1,3] resulting in a much higher density of Ni islands (with usually incoherent lattices due to the incommensurate adlattice structure).

4.3. Ni nucleation and growth

The results described in section 3.2 reveal several remarkable aspects about the electrochemical growth of Ni on Ag(111): (i) the amount of deposited material along the steps is independent of the size of the neighboring terraces, indicating that material transport from the terraces does not contribute significantly to the island growth; (ii) a crossover from two-dimensional to a three-dimensional Ni growth occurs with increasing overpotential and (iii) the shape of the Ni islands depends on the overpotential. These aspects as well as the role of structural defects on the Ni nucleation and growth will be discussed in this section.

The first effect can be explained by a "direct deposition" mechanism, where Ni^{2+} ions can only be discharged (and subsequently incorporated) at step or kink sites, but not, or at a much lower rate, at sites on the terraces, due to substantially different activation barriers for the ion transfer reaction at the two types of sites. The role of direct transfer in metal deposition processes was first recognized by Gerischer, based on theoretical considerations.[62] Noteworthy among the rare experimental confirmations of this mechanism are the optical microscopy studies of Ag homoepitaxial deposition on Ag(100) electrodes by Bostanov *et al.*, where the propagation rate of Ag multilayer steps was found to be independent of the step height.[63] Direct transfer is believed to be a general phenomenon in electrochemical metal deposition and dissolution. It is commonly assumed, however, that it accounts for only a fraction of the deposited atoms and that a significant contribution results from atoms, which are deposited as adatoms on the terraces.[45] Our results, which show an identical amount of deposited Ni for steps with adjacent terraces differing by a factor 10 or more, indicate a different scenario for Ni electrodeposition on Ag(111), with the Ni islands being almost exclusively formed *via* direct deposition and the deposition *via* adatoms being rather small. On the other hand, direct deposition alone cannot account for the observed Ni place exchange on the Ag terraces, which indicates that even at low overpotentials Ni adatom deposition is not completely impossible. For molecular beam epitaxial growth under UHV conditions direct deposition is of course not possible. Consequently, UHV-STM results for Ni on Ag(111) show a clear influence of the width of the neighboring terraces on the Ni island size.[52] The direct transfer mechanism in the electrochemical environment can hence improve the homogeneity of the deposited islands on the μm scale and reduce the sensitivity of the island size on the substrate morphology, an effect which may be useful for the controlled preparation of metal nanostructures.

The crossover from 2D to 3D growth can be rationalized in a simple kinetic model where the (direct) deposition at various surface sites is assumed to depend differently on the deposition potential. In this model we consider Ni deposition at three different surface sites—Ni step edges on the Ag substrate, Ni step edges on the Ni adlayer, and the defect sites on top of the Ag/Ni boundary (see Fig. 11a)—which define the lateral growth rate of the first Ni layer on Ag $k_{Ni/Ag}$, the lateral growth rate of the second and higher Ni layers on top of Ni islands $k_{Ni/Ni}$, and the rate of next-layer nucleation k_{nucl} (see below), respectively. The Ni deposition rates $k_{Ni/Ag}$ (Fig. 11b, solid line) and $k_{Ni/Ni}$ (Fig. 11b, dashed line) are assumed to exhibit a Tafel behavior, *i.e.*, $k_{Ni/X} \propto \exp(a_{Ni/X}\eta)$ with X = Ag, Ni, where $a_{Ni/X}$ are the Tafel slopes. Furthermore, we assume that the rate for the (heterogeneous) nucleation of second- or higher-layer admetal islands k_{nucl}, required for multilayer growth, is negligibly small as compared to $k_{Ni/Ag}$ at the onset of Ni deposition, but increases much more rapidly with overpotential, either due to a larger Tafel slope (Fig. 11b, dotted line) or due to a completely different potential dependence, *e.g.*, $k_{nucl} \propto \exp(-a_{nucl}\eta^{-1})$,[45] and finally becomes comparable or even larger than $k_{Ni/Ag}$. In this case, nucleation on top of the Ni–Ag boundary is kinetically hindered at low η (regime I in Fig. 11b), resulting in the predominantly lateral growth of a flat deposit. At higher η (regime II) the next-layer nucleation rate k_{nucl}, *i.e.*, the vertical island growth rate,

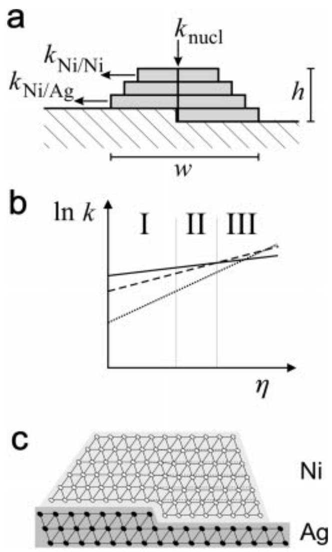

Fig. 11 Schematic illustration of (a) the Ni island geometry and the elementary nucleation and lateral growth processes, (b) the dependence of the rate of the different processes on overpotential, with $k_{Ni/Ag}$, $k_{Ni/Ni}$ and k_{nucl} indicated by solid, dashed, and dotted lines, respectively, and (c) the structural defect at the Ni–Ag boundary caused by the difference in atomic radius between Ni and Ag.

increases and multilayer islands are formed. A similar variation of the initial (first layer) island nucleation rate could explain the increase in Ni island density along the steps with increasing overpotential.

With the above model the change in the Ni island shape with overpotential can also be rationalized. The increase in aspect ratio with η is a direct consequence of the faster increase of the vertical (*i.e.*, k_{nucl}) as compared to the lateral growth rate (*i.e.*, $k_{Ni/Ag}$). Furthermore, the change from a "trapezoidal" island cross-section at medium η to an almost "rectangular" one at high η can be attributed to a different potential dependence of the Ni growth rate on Ag ($k_{Ni/Ag}$) and on existing Ni islands ($k_{Ni/Ni}$): At low η the lateral growth of second and higher layer Ni islands on the underlying Ni layer proceeds rather slowly, *i.e.*, $k_{Ni/Ni} \leqslant k_{Ni/Ag}$, leading to a "trapezoidal" shape. In contrast, at high η (regime III in Fig. 11b) the "rectangular" island shape indicates a much faster Ni growth on Ni islands than on the Ag substrate (*i.e.*, $k_{Ni/Ni} \gg k_{Ni/Ag}$), where the second and higher layers spread rapidly across the entire Ni island. The lateral island size is then determined by the growth rate of the first layer. According to this scenario, the relatively uniform width of the multilayer islands does not result from an intrinsic limitation (*e.g.*, strain effects) but solely from the growth kinetic.

At low or medium overpotentials nucleation of second Ni layer islands occurs almost exclusively at the structural defect given by the Ni–Ag boundary. The lattice distortion induced by this boundary also continues into the second and higher Ni layer, however, it is gradually removed with increasing island thickness due to lattice relaxations (Fig. 11c). Consequently, the probability for heterogeneous nucleation at this position should continuously decrease with increasing island height, resulting in a crossover to a more lateral growth. This is in good agreement with the STM data, which find this crossover at a thickness of 5 to 6 layers. Interestingly, the same length scale was found for the vertical relaxation of the periodic lattice distortion induced by the Ag–Ni lattice mismatch, *i.e.*, the moiré pattern (see section 4.2). The observed change of average height and width as a function of deposition time (Fig. 6) can be quantitatively described by a simple two-dimensional model, which is presented in the Appendix. Furthermore, this nucleation and growth behavior is also in good agreement with the EQCM data (Fig. 2b), which show a slow increase in deposition rate at short deposition times, reflecting the nucleation and vertical island growth, and a constant deposition rate at longer times, where the islands grow predominantly lateral onto terraces (*i.e.*, *via* deposition at an approximately constant number of step sites). Preferential nucleation at the positions of substrate steps, although less exclusively, was also reported for the electrodeposition of Cu on Au(111)[64] and Au(100)[65] and of Ni on Au(111),[3] suggesting that this is a quite common phenomenon in electrodeposition. In addition, our STM observations reveal that next-layer Ni islands occasionally also nucleate at the Ni island edges. This behavior might be caused by the formation of a Ni–Ag boundary at these edges due to (partial) encapsulation of the Ni islands by Ag surface atoms. The latter effect can be directly observed in time-resolved series of STM images and is discussed in detail in ref. 37.

At high overpotentials Ni multilayer islands not only form along the steps, but also within the terraces of the Ag substrate. This might be attributed simply to homogeneous nucleation or to an alternative mechanism, proposed in an STM study of Ni deposition on Ag(111) under UHV conditions, where a very similar morphology was found.[52,54] In this study the formation of islands within the terraces was explained by two effects: At low temperatures the Ni islands apparently form *via* homogeneous nucleation, whereas at elevated temperatures heterogeneous nucleation on top of substitutional Ni atoms within the Ag surface layer was suggested. Since a transition temperature between 300 and 400 K was estimated in that study, a significant contribution by both of these processes is expected at room temperature. Our STM results indicate that, similar as under UHV conditions, substitution of Ag surface atoms by Ni *via* a place exchange mechanism also occurs (at all overpotentials) in the electrochemical environment. For this reason, it is not unlikely that the formation of multilayer islands during electrodeposition at high η is (partly) caused by this heterogeneous nucleation mechanism. At low or medium overpotentials, in contrast, the stabilization of Ni island nuclei by substitutional Ni atoms seems to be too small, *e.g.*, due to a lower Ni adatom density on the terraces.

The complex behavior found in this system, especially the transition from two-dimensional step-flow to selective nucleation and growth of 3D islands at steps to 3D growth at steps and on terraces with increasing overpotential, can be employed for the controlled preparation of admetal structures with well-defined nanometer scale morphology. In particular the magnetic and electronic properties of such nanostructured Ni/Ag surfaces are of potential interest, since composite systems of ferromagnetic and nonmagnetic metals with dimensions in the nm range often exhibit unusual behavior, such as giant magnetoresistance. Compared to previous magnetic nanostructures,[66] Ni electrodeposits on Ag(111) may offer various advantages. First, the size of the resulting Ni multilayer islands is rather uniform on the μm scale, since the dimensions of the deposited islands do not depend on the size of the adjacent terraces and the height of the deposits is relatively uniform due to the "self-limiting" vertical growth. Second, the formation of Ni "nanowires" along the steps is highly selective and can be easily achieved at deposition potentials between −0.77 and −0.84 V *vs.* SCE. As found in recent studies,[67] Ni "nanowires" with very defined spacing, *i.e.*, highly anisotropic deposits, can be prepared by deposition on vicinal Ag surfaces.

4.4. Dissolution mechanism

The anodic dissolution of the Ni deposit on Ag(111) proceeds *via* a step-flow mechanism, with a non-uniform etch rate along the Ni island edges. In stark contrast, the dissolution of ultrathin Ni films on Au(111) electrodes proceeds *via* formation of multilayer pits (usually reaching down to the Au substrate) and their subsequent lateral growth,[3] despite the identical Ni lattice structure. We attribute this difference to the considerably higher defect density in the Ni deposit on Au(111) as compared to that on Ag(111) (see section 4.2). Apparently, the incoherent domain boundaries between the Ni grains can act as pit nucleation sites. For bulk (oxide free) Ni(111) an intermediate behavior was reported in *in situ* STM studies of the dissolution process in sulfuric acid solution:[68–71] While in some studies a step flow etching was found at low dissolution rates,[68,71] in other cases, in particular at higher rates, the formation of pits was observed.[69–71] In analogy to our observations on epitaxial Ni(111) films, formation of pits might also on bulk Ni(111) be related to the presence of structural defects. In addition, the STM observations show that the dissolution rate for the bottom Ni layer, *i.e.*, the layer at the Ni/Ag interface, is higher than that of the second and higher Ni layers. This can be explained by a less favorable Ni–Ag interaction as compared to the interaction between Ni atoms (see section 4.5).

4.5. Admetal–substrate interaction

The nucleation and growth of Ni islands is accompanied by significant changes in the Ag(111) substrate. As shown in ref. 37, these can be rationalized by a partial encapsulation of the Ni islands *via* Ag surface atom diffusing along the Ag step edges. In a similar way, the changes in the Ag substrate upon dissolution of the Ni deposit can be attributed to a release of the Ag atoms surrounding the Ni islands. The tendency for encapsulation is in agreement with the observed place exchange of Ni with Ag surface atoms and was also found for Ni on Ag(111) under UHV conditions.[52] The STM data strongly indicate, however, that the Ni islands are not completely encapsulated, but that Ag atoms attach solely along the island edges. If the top of the islands would be covered by a Ag layer the moiré pattern amplitude would be independent of the island thickness rather than decay with increasing layer number, as observed experimentally.

The observed tendency towards Ni island encapsulation indicates a stronger bonding of Ag atoms to the Ni deposit than to the Ag substrate. On the other hand, a less favorable Ni–Ag interaction as compared to the interaction between Ni atoms is required to rationalize the EQCM measurements, the growth behavior at medium and high overpotentials, and the dissolution behavior. Both conditions can be fulfilled simultaneously only if the bond energies decrease in the order Ni–Ni > Ni–Ag > Ag–Ag. Support for this sequence comes from thermodynamic data, which report a higher crystal lattice enthalpy (ΔH^{298}(Ni gas) = 429.7 kJ mol^{-1}, (ΔH^{298}(Ag gas) = 284.9 kJ mol^{-1}) as well as a higher diatomic bond energy ($E_{\mathrm{Ni-Ni}}$ = 203 kJ mol^{-1}, $E_{\mathrm{Ag-Ag}}$ = 163 kJ mol^{-1}) for Ni than for Ag.[72] Furthermore, a simple estimate of the Ni–Ag interaction energy from the lattice enthalpies and the enthalpy of mixing (0.8 eV^{-1} atom^{-1}[41]), where the latter is assumed to depend only on the bond energy differences between nearest neighbors, gives a value in between those of Ni–Ni and Ag–Ag. These trends are in agreement with density functional calculations, which indicate pronounced segregation of Ni into Ag(111).[73]

5. Conclusion

We have presented a comprehensive *in situ* STM, EQCM, and electrochemical study of Ni deposition and dissolution on Ag(111) electrodes, which gives detailed insight into the structure and morphology of the Ni deposit, the underlying nucleation and growth processes, and the interactions of Ni and Ag substrate atoms. In summary, the following results were obtained:

Ni electrodeposition on Ag(111) requires nucleation overpotentials $\eta \geqslant 160$ mV, which is significantly higher than for Ni deposition on Au(111). This may be related to the higher energetic cost for the formation of the substrate–admetal interface or the more negative potential of zero charge of Ag.

The Ni deposit exhibits a well-ordered, (111)-oriented, incommensurate lattice, with the Ni adlayer being slightly rotated ($\approx 0.5°$) with respect to the Ag substrate lattice. Whereas the in-plane atomic spacing in Ni islands of three or more layers thickness is close to that of bulk Ni (2.49 Å), an expanded lattice is found for monolayer (2.52 Å) and bilayer (2.54 Å) Ni islands.

With increasing overpotential three different growth regimes with different deposit morphologies are found: 2D step-flow growth of a smooth Ni film (160 mV $\leqslant \eta \leqslant$ 200 mV), selective 3D island growth along the Ag steps (200 mV $\geqslant \eta \geqslant$ 300 mV), and 3D island growth along the steps and on the terraces of the Ag substrate ($\eta \geqslant$ 300 mV). The transformation from 2D to 3D growth can be rationalized by a more rapid increase in the rate of next-layer nucleation (*i.e.*, vertical island growth rate) than the lateral island growth rate. This model can also explain the dependence of the island shape on the overpotential.

The island dimensions are independent of the local substrate morphology, in particular of the width of the neighboring Ag terraces, indicating that Ni direct discharge at step sites plays an important role in Ni deposition.

Based on the observation that next-Ni-layer nucleation proceeds predominantly at the structural defects induced by the

Ni–Ag boundary in the bottom layer, the growth and shape evolution of the Ni multilayer islands on top of the Ag steps can be described quantitatively.

The Ni film dissolves *via* a step-flow mechanism, with a non-uniform etch rate along the Ag steps. The dissolution rate for Ni monolayer islands is higher than that of second and higher Ni layer islands, which might be explained by a lower stability of the Ni monolayer caused by the energetically unfavorable Ag/Ni interface.

Ni electrodeposition and dissolution is accompanied by a substantial rearrangement of the Ag substrate. This can be attributed to pronounced Ni–Ag interactions, such as place exchange of Ni with Ag surface atoms and partial encapsulation of Ni islands by Ag, as also found for Ni deposition on Ag(111) under UHV conditions.

In summary, Ni electrodeposition on Ag(111) exhibits a complex, potential-dependent growth behavior, which may offer interesting opportunities for the controlled formation of nanostructured electrode surfaces.

Acknowledgement

We are grateful for a fellowship from the Alexander von Humboldt foundation (S.M.), as well as for the financial support and a fellowship (O.M.M.) by the Deutsche Forschungsgemeinschaft.

Appendix: island growth model

To describe the average height and the aspect ratio of the Ni multilayer islands on top of the Ag steps as a function of deposition time (see Fig. 6), we have developed a simple model where only island growth along the surface-normal direction and perpendicular to the step (*i.e.*, in the plane shown in Fig. 11a and c) is considered and growth along the step direction is neglected. In this model we assume that the nucleation of the next Ni layer, which defines the vertical island growth rate $\mathrm{d}h/\mathrm{d}t$, occurs exclusively at the structural defect in the Ni surface layer, induced by the Ag–Ni boundary in the bottom layer. The probability for this heterogeneous nucleation process is assumed to decrease with increasing island height due to the gradual relaxation of the Ni lattice (see Fig. 11c), as described in the following.

On top of the Ag–Ni boundary, *i.e.*, the former Ag step, the vertical mismatch of Ag and Ni lattice produces a strain field in the deposit which resembles that produced by dislocation lines in a solid crystal. It can be estimated using continuum elasticity theory. According to this theory the strain u in the top Ni layer directly above the Ag–Ni boundary decays inversely proportional to the distance to the topological defect,[74] *i.e.*, with the Ni island thickness h:

$$u \propto h^{-1}$$

We further assume that the adatom binding energy E and the hopping barrier for surface diffusion E_{diff} (*i.e.*, the relevant energy terms for the formation of a critical nucleus of size $i = 0$ and $i = 1$, respectively) depend linearly on the lattice strain u, as recently shown by density functional calculations for Ag adatoms on strained Ag(111) and Pt(111) substrates:[75]

$$E = E_0 + E_{\mathrm{strain}} = E_0 + K'u = E_0 + K''h^{-1}$$

$$E_{\mathrm{diff}} = E_{\mathrm{diff,\,0}} + E_{\mathrm{diff,\,strain}} = E_{\mathrm{diff,\,0}} + K'''h^{-1}$$

with K' and K'' being constants. Assuming a critical nucleus of size $i = 0$,[45] the nucleation rate at the defect site is given by:[76–78]

$$v = v_0 \exp\left(\frac{E}{kT}\right) = v_0 \exp\left(\frac{E_0}{kT}\right)\left(\frac{K''}{kT}\frac{1}{h}\right)$$

Similar results are obtained for critical nuclei $i > 0$, where the exponent is modified by an energy term resulting from the diffusion barrier.[76–78]

On the other hand, the next-layer nucleation rate v is identical to the vertical island growth rate $\mathrm{d}h/\mathrm{d}t$, *i.e.*:

$$\frac{\mathrm{d}h}{\mathrm{d}t} = v_0 \exp\left(\frac{K''}{kT}\frac{1}{h}\right) = v_0 \exp\left(\frac{a}{h}\right); \quad a \equiv \frac{K''}{kT}$$

which can be easily solved as (Ei being the exponential integral):

$$t(h) = \int v_0^{-1} \exp\left(-\frac{a}{h}\right)\mathrm{d}h = \frac{a}{v_0}\left[\frac{h}{a}\exp\left(-\frac{a}{h}\right) - \mathrm{Ei}\left(1, \frac{a}{h}\right)\right]$$

This relation provides a good fit to the experimentally observed island growth behavior (Fig. 6) for $\langle h \rangle \geqslant 3$ for an additional strain-induced energy $E_{\mathrm{strain}} = K''h^{-1} = 130$ meV h^{-1} for nucleation on top of an h-layer-thick Ni deposit (solid line in Fig. 6). With increasing deposit height this additional energy should asymptotically approach zero, corresponding to an increasingly homogeneous next-layer nucleation. In contrast to the vertical growth rate, the rate of lateral island growth, $k_{\mathrm{Ni/Ag}}$, is independent of the island thickness, resulting in an increasing aspect ratio $\langle w \rangle/\langle h \rangle$ with height. The deviation of the fit from the experimental data for $\langle h \rangle < 3$ layers is not surprising in view of the employed approximation of the strain by continuum elasticity theory, which should break down for distances of a few atomic spacings.

References

1 F. A. Möller, O. M. Magnussen and R. J. Behm, *Phys. Rev. Lett.*, 1996, **77**, 5249.
2 F. A. Möller, O. M. Magnussen and R. J. Behm, *Phys. Rev. Lett.*, 1996, **77**, 3165.
3 F. A. Möller, J. Kintrup, A. Lachenwitzer, O. M. Magnussen and R. J. Behm, *Phys. Rev. B*, 1997, **56**, 12506.
4 F. A. Möller, O. M. Magnussen and R. J. Behm, *Z. Phys. Chem.*, 1999, **208**, 57.
5 O. M. Magnussen and R. J. Behm, *J. Electroanal. Chem.*, 1999, **467**, 258.
6 S. Morin, A. Lachenwitzer, F. A. Möller, O. M. Magnussen and R. J. Behm, *J. Electrochem. Soc.*, 1999, **146**, 1013.
7 S. Morin, A. Lachenwitzer, O. M. Magnussen and R. J. Behm, *Phys. Rev. Lett.*, 1999, **83**, 5066.
8 A. Lachenwitzer, M. R. Vogt, O. M. Magnussen and R. J. Behm, *Surf. Sci.*, 1997, **382**, 107.
9 S. K. Verma and H. Wilman, *J. Phys. D*, 1971, **4**, 1167.
10 A. Vértes, I. Czakó-Nagy, M. Lakatos-Varsányi, L. Csordás and H. Leidheiser, Jr., *J. Electrochem. Soc.*, 1984, **131**, 1522.
11 A. Vértes, C. Szeles, Z. Kajcsos and H. Leidheiser, Jr., *J. Electrochem. Soc.*, 1984, **131**, 1526.
12 K.-M. Yin and B.-T. Lin, *Surf. Coat. Technol.*, 1996, **78**, 205.
13 M. Y. Abyaneh and M. Fleischmann, *J. Electroanal. Chem.*, 1981, **119**, 187.
14 M. Y. Abyaneh and M. Fleischmann, *J. Electroanal. Chem.*, 1981, **119**, 197.
15 I. Epelboin, M. Joussellin and R. Wiart, *J. Electroanal. Chem.*, 1981, **119**, 61.
16 M. Fleischmann and A. Saraby-Reintjes, *Electrochim. Acta*, 1984, **29**, 69.
17 E. Gómez, C. Müller, W. G. Proud and E. Vallés, *J. Appl. Electrochem.*, 1992, **22**, 872.
18 E. Gómez, R. Pollina and E. Vallés, *J. Electroanal. Chem.*, 1995, **386**, 45.
19 E. Gómez, R. Pollina and E. Vallés, *J. Electroanal. Chem.*, 1995, **397**, 111.
20 W. G. Proud and C. Müller, *Electrochim. Acta*, 1993, **38**, 405.
21 W. G. Proud, E. Gómez, E. Sarret, E. Vallés and C. Müller, *J. Appl. Electrochem.*, 1995, **25**, 770.
22 C. Bozhkov, C. Tzvetkova, S. Rashkov, An. Budniok and A. Budniok, *J. Electroanal. Chem.*, 1990, **296**, 453.

23 M. Zhou, N. Myung, X. Chen and K. Rajeshwar, *J. Electroanal. Chem.*, 1995, **398**, 5.
24 T. C. Franklin and S. A. Mathew, *J. Electrochem. Soc.*, 1988, **135**, 2725.
25 M. Benje, M. Eiermann, U. Pittermann and K. G. Weil, *Ber. Bunsen-Ges. Phys. Chem.*, 1986, **90**, 435.
26 J. P. Hoare, *J. Electrochem. Soc.*, 1986, **133**, 2491.
27 J. P. Hoare, *J. Electrochem. Soc.*, 1987, **134**, 3102.
28 T. Mimani, S. M. Mayanna and N. Munichandraiah, *J. Appl. Electrochem.*, 1993, **23**, 339.
29 C.-C. Cheng and A. C. West, *J. Electrochem. Soc.*, 1997, **144**, 3050.
30 J. Horkans, *J. Electrochem. Soc.*, 1979, **126**, 1861.
31 J. Ji, W. C. Cooper, D. B. Dreisinger and E. Peters, *J. Appl. Electrochem.*, 1995, **25**, 642.
32 N. Zech and D. Landolt, *Electrochim. Acta*, 2000, **45**, 3461.
33 C. Arkam, V. Bouet, C. Gabrielli, G. Maurin and H. Perrot, *J. Electrochem. Soc.*, 1994, **141**, L103.
34 N. Lebbad, J. Voiron, B. Nguyen and E. Chainet, *Ann. Chim. Fr.*, 1995, **20**, 391.
35 A. Lachenwitzer and O. M. Magnussen, *J. Phys. Chem. B*, 2000, **104**, 7424.
36 J. L. Bubendorff, L. Cagnon, V. Costa-Kieling, J. P. Bucher and P. Allongue, *Surf. Sci.*, 1997, **384**, L836.
37 F. Maroun, S. Morin, A. Lachenwitzer, O. M. Magnussen and R. J. Behm, *Surf. Sci.*, 2000, **460**, 249.
38 J. Morales, S. M. Krijer, P. Esparza, S. González, L. Vázquez, R. C. Salvarezza and A. J. Arvia, *Langmuir*, 1996, **12**, 1068.
39 T. P. Moffat, *Mater. Res. Soc. Symp. Proc.*, 1996, **404**, 3.
40 A. Hamelin, T. Vitanov, E. Sevastyanov and A. Popov, *J. Electroanal. Chem.*, 1983, **145**, 225.
41 F. R. de Boor, R. Boom, W. C. M. Mattens, A. R. Miedema and A. K. Niessen, *Cohesion in Metals: Transition Metal Alloys*, North Holland, Amsterdam, 1988.
42 A. Lachenwitzer, PhD Thesis, University of Ulm, 2000.
43 T. Kurasawa, *Chem. Abs.*, 1961, **55**, 14279.
44 A. Hamelin, personal communication, 1990.
45 E. Budevski, G. Staikov and W. J. Lorenz, *Electrochemical Phase Formation and Growth: An Introduction to the Initial Stages of Metal Deposition*, VCH Verlagsgesellschaft mbH, Weinheim, 1996.
46 G. N. Salaita, F. Lu, L. Laguren-Davidson and A. T. Hubbard, *J. Electroanal. Chem.*, 1987, **229**, 1.
47 M. S. Zei, *J. Electroanal. Chem.*, 1991, **308**, 295.
48 G. Aloisi, A. M. Funtikov and T. Will, *J. Electroanal. Chem.*, 1994, **370**, 294.
49 A. Saraby-Reintjes and M. Fleischmann, *Electrochim. Acta*, 1984, **29**, 557.
50 M. Dietterle, T. Will and D. M. Kolb, *Surf. Sci.*, 1995, **327**, L495.
51 M. Giesen, M. Dietterle, D. Stapel, H. Ibach and D. M. Kolb, *Surf. Sci.*, 1997, **384**, 168.
52 P. Schmid, PhD Thesis, University of Ulm, 1995.
53 J. A. Meyer, I. D. Baikie, E. Kopatzki and R. J. Behm, *Surf. Sci.*, 1996, **365**, L647.
54 J. A. Meyer and R. J. Behm, *Surf. Sci.*, 1995, **322**, L275.
55 D. Marcu, H. Hall, S. Patel and S. Morin, in preparation.
56 Z. Shi and J. Lipkowski, *J. Electroanal. Chem.*, 1996, **403**, 225.
57 M. F. Toney, J. G. Gordon, G. L. Borges, O. R. Melroy, D. Yee and L. B. Sorensen, *Phys. Rev. B*, 1994, **49**, 7793.
58 C. Günther, J. Vrijmoeth, R. Q. Hwang and R. J. Behm, *Phys. Rev. Lett.*, 1995, **74**, 754.
59 M. F. Toney, J. G. Gordon, M. G. Samant, G. L. Borges, O. R. Melroy, D. Yee and L. B. Sorensen, *Phys. Rev. B*, 1992, **45**, 9362.
60 J. X. Wang, R. R. Adzic, O. M. Magnussen and B. Ocko, *Surf. Sci.*, 1995, **344**, 111.
61 D. D. Chambliss, R. J. Wilson and S. Chiang, *J. Vac. Sci. Technol. B*, 1991, **9**, 933.
62 H. Gerischer, in *Proceedings of International Conference on Protection against Corrosion by Metal Finishing*, ed. N. Ibl, K. M. Oesterle and A. Saboz, Forster, Zuerich, 1967, p. 199.
63 G. Bostanov, G. Staikov and D. K. Roe, *J. Electrochem. Soc.*, 1975, **122**, 1301.
64 R. J. Nichols, D. M. Kolb and R. J. Behm, *J. Electroanal. Chem.*, 1991, **313**, 109.
65 N. Batina, D. M. Kolb and R. J. Nichols, *Langmuir*, 1992, **8**, 2572.
66 H. J. Elmers, J. Hauschild, H. Höche, U. Gradmann, H. Bethge, D. Heuer and U. Köhler, *Phys. Rev. Lett.*, 1994, **73**, 898.
67 S. Morin and A. Lachenwitzer, personal communication, 2000.
68 T. Suzuki, T. Yamada and K. Itaya, *J. Phys. Chem.*, 1996, **100**, 8954.
69 D. Zuili, V. Maurice and P. Marcus, *Electrochem. Soc. Proc.*, 1997, **97-26**, 1013.
70 D. Zuili, V. Maurice and P. Marcus, *J. Electrochem. Soc.*, 2000, **147**, 1393.
71 J. Scherer, B. Ocko and O. M. Magnussen, in preparation.
72 *Handbook of Chemistry and Physics*, ed. R. C. Weast, CRC Press, Boca Raton, FL, 76th edn., 1995.
73 A. V. Ruban, H. L. Skriver and J. K. Nørskov, *Phys. Rev. B*, 1999, **59**, 15990.
74 P. M. Chainkin and T. C. Lubensky, *Principles of Condensed Matter Physics*, Cambridge University Press, Cambridge, 1995.
75 C. Ratsch, A. P. Seitsonen and M. Scheffler, *Phys. Rev. B*, 1997, **55**, 6750.
76 J. A. Venables, G. D. T. Spiller and M. Hanbrücken, *Rep. Prog. Phys.*, 1984, **47**, 399.
77 J. A. Venables, *J. Vac. Sci. Technol. B*, 1986, **4**, 870.
78 J. A. Venables, *Surf. Sci.*, 1994, **299/300**, 798.